

Research Article

Open Access



# Constructing a hierarchical MoS<sub>2</sub>/MXene heterostructure for efficient capacitive deionization of saline water

Youfang Zhang<sup>1</sup>, Xin Li<sup>1</sup>, Wen Xi<sup>2</sup>, Qi Zhang<sup>1</sup>, Xiaohui Ge<sup>1</sup>, Jun You<sup>1</sup>, Qunchao Zhang<sup>1</sup>, Dean Shi<sup>1\*</sup>, Jun Jin<sup>2\*</sup>

<sup>1</sup>Hubei Key Laboratory of Polymer Materials, Ministry of Education Key Laboratory for Green Preparation and Application of Functional Materials, School of Materials Science and Engineering, Hubei University, Wuhan 430062, Hubei, China.

<sup>2</sup>Faculty of Materials Science and Chemistry, China University of Geosciences, Wuhan 430074, Hubei, China.

\***Correspondence to:** Prof. Dean Shi, Hubei Key Laboratory of Polymer Materials, Ministry of Education Key Laboratory for Green Preparation and Application of Functional Materials, School of Materials Science and Engineering, Hubei University, 368 Youyi Avenue, Wuchang District, Wuhan 430062, Hubei, China. E-mail: deanshi2012@hubu.edu.cn; Prof. Jun Jin, Faculty of Materials Science and Chemistry, China University of Geosciences, 388 Lumo Road, Hongshan District, Wuhan 430074, Hubei, China. E-mail: jinjun@cug.edu.cn

**How to cite this article:** Zhang Y, Li X, Xi W, Zhang Q, Ge X, You J, Zhang Q, Shi D, Jin J. Constructing a hierarchical MoS<sub>2</sub>/MXene heterostructure for efficient capacitive deionization of saline water. *Chem Synth* 2024;4:19. <https://dx.doi.org/10.20517/cs.2023.37>

**Received:** 28 Jul 2023 **First Decision:** 17 Jan 2024 **Revised:** 20 Feb 2024 **Accepted:** 28 Feb 2024 **Published:** 1 Apr 2024

**Academic Editor:** Xiang-Dong Yao **Copy Editor:** Dong-Li Li **Production Editor:** Dong-Li Li

## Abstract

Well-dispersed and few-layered molybdenum disulfide (MoS<sub>2</sub>) has been considered as a suitable electrode material for pseudocapacitive capacitive deionization (CDI) due to its lamellar structure, flexible interlayer intercalation, and high theoretical capacity. However, the serious aggregation, low electrical conductivity and poor hydrophilicity of MoS<sub>2</sub> have limited its desalination application. To address these issues, few-layered MXene is used as a conductive and hydrophilic skeleton to support MoS<sub>2</sub> nanosheets. In this study, a hierarchical MoS<sub>2</sub>/MXene heterostructure is fabricated for highly efficient CDI of saline water. The designed heterostructure effectively inhibits the agglomeration of MoS<sub>2</sub> and MXene nanosheets, exposes more active electrochemical sites, and improves the wettability, thereby enhancing ion/charge transport. The MoS<sub>2</sub>/MXene heterostructure electrode exhibits low electrical resistance (3.2 Ω), along with a high specific capacitance of 171.8 F·g<sup>-1</sup> at 2 A·g<sup>-1</sup>. Furthermore, the MoS<sub>2</sub>/MXene-based CDI electrode demonstrates an excellent desalination capacity of 55.8 mg·g<sup>-1</sup> and a fast desalination rate of 13 mg·g<sup>-1</sup>·min<sup>-1</sup>. This study paves the way for novel applications in the CDI field.

**Keywords:** Capacitive deionization, MXene, MoS<sub>2</sub>, wettability, desalination



© The Author(s) 2024. **Open Access** This article is licensed under a Creative Commons Attribution 4.0 International License (<https://creativecommons.org/licenses/by/4.0/>), which permits unrestricted use, sharing, adaptation, distribution and reproduction in any medium or format, for any purpose, even commercially, as long as you give appropriate credit to the original author(s) and the source, provide a link to the Creative Commons license, and indicate if changes were made.



## INTRODUCTION

In recent years, the indiscriminate discharge of industrial wastewater, the misuse of various chemical fertilizers and pesticides, and other harmful substances to the environment have led to an increasing pollution of water sources, resulting in a scarcity of freshwater resources. Exploring highly efficient seawater/brackish desalination techniques is a crucial strategy to address the freshwater shortage. However, traditional desalination techniques, such as pressure-driven desalination, thermal-driven desalination and electric-driven desalination, are hindered by the challenges including high cost, excessive energy consumption, and issues related to secondary pollution. These limitations make them unsuitable for practical applications<sup>[1-3]</sup>. Capacitive deionization (CDI), as a novel and emerging desalination technique, is characterized by easy operation, cost-effectiveness, minimal energy consumption, and eco-friendly features, making it highly promising for seawater desalination and heavy metal removal<sup>[4,5]</sup>.

The CDI process is typically categorized into two main stages: adsorption and desorption<sup>[6]</sup>. During the adsorption stage, a positive voltage is applied to CDI. Cations and anions in saltwater move towards negative and positive electrodes, respectively, due to the applied electrostatic field. These results in the ions being adsorbed onto the surface or pores of electrode materials. In the desorption stage, the ions adsorbed on electrode materials are released back into water when the charge is removed or reversed<sup>[7]</sup>. The key CDI components are the electrode materials, which can be categorized into double-layer capacitance materials (e.g., graphene, carbon nanotubes, and carbon aerogels)<sup>[5,8-11]</sup> and faradic electrode materials (e.g., transition metal oxides/sulfides and magnesium titanate)<sup>[12-15]</sup>. The double-layer capacitance materials primarily rely on ion storage to remove salts from water, leading to insufficient desalination capacity, non-selective adsorption of anions and cations, and anode corrosion<sup>[16]</sup>. In addition, co-ion repulsion effects and side reactions in these materials result in relatively low charge utilization efficiency. To address these limitations, novel faradic electrode materials, such as transition metal oxides, sulfides, carbides, redox-active polymers, and Prussian blue, have been prepared to improve the inherent desalination performances<sup>[17-22]</sup>.

MXene is a novel family of 2D materials composed of transition-metal layers interleaved with carbide/nitride ones<sup>[23]</sup>. It is commonly prepared by selectively removing the “A” layer from the MAX phase through etching. In the general formula of  $M_{n+1}AX_n$  ( $n = 1, 2, 3$ ), “M” shows a transition metal. “A” represents Al or Si, while “X” signifies C, N, or C and N. In  $M_{n+1}X_nT_x$ , “T<sub>x</sub>” represents hydroxyl-, oxygen-, or fluorine-terminated groups on the surface. MXene possesses excellent conductivity attributed to its metallic nature. Additionally, it exhibits high specific surface area and good hydrophilicity thanks to the termination of -OH, -O and -F groups<sup>[11,19]</sup>. Furthermore, MXene showcases adjustable lamellar structure, which can offer sufficient space for anchoring electrochemically active nanoparticles on the surface and interlayer<sup>[24-31]</sup>. These characteristics make it an excellent candidate for CDI electrode materials. However, similar to other 2D materials, MXene nanosheets have the agglomeration and restack problem as a result of van der Waals interactions, leading to a reduction in interlayer spacing, limiting ion transport, and hindering sufficient contact between the nanosheets and electrolyte. As a result, the actual performances of MXene in CDI are far lower than its theoretical capability.

Molybdenum disulfide ( $MoS_2$ ) is a typical 2D layered material composed of two hexagonal nanosheets (S atoms) and one intermediate hexagonal sheet (Mo atoms). The weak van der Waals force between neighboring layers of  $MoS_2$  can enhance ion adsorption and transport.  $MoS_2$ -based electrodes have shown excellent CDI performance in capturing sodium ions from salt water<sup>[12,32-37]</sup>. However, the serious structural aggregation, inferior electrical conductivity, and poor hydrophilicity of  $MoS_2$  greatly limit its desalination performance.

In this work, few-layered MXene is utilized as a robust, conductive and hydrophilic skeleton to support MoS<sub>2</sub> nanosheets for the fabrication of hierarchical MoS<sub>2</sub>/MXene heterostructures. The designed MoS<sub>2</sub>/MXene heterostructures can prevent the aggregation of both MXene and MoS<sub>2</sub> nanosheets and provide a rich exposure of active sites, expanded MXene interlayer spacing, and suitable wettability, enabling fast ion diffusion. As a result, the optimized MoS<sub>2</sub>/MXene device for CDI exhibits an excellent desalination capacity of 55.8 mg·g<sup>-1</sup> at a voltage of 1.2 V. Therefore, high conductivity and hydrophilicity MXene-supported nanosized MoS<sub>2</sub> shows great promise as a low-cost electrode material in the field of CDI.

## EXPERIMENTAL SECTION

### Preparation of MXene nanosheets

MXene nanosheets are prepared by selectively eliminating the Al layer from Ti<sub>3</sub>AlC<sub>2</sub> in an HF aqueous solution, following the method reported in our prior work<sup>[38]</sup>. The specific procedures can be found in the [Supplementary Materials](#).

### Synthesis of MoS<sub>2</sub>/MXene heterostructures

The hierarchical MoS<sub>2</sub>/MXene heterostructures are synthesized using a straightforward solvothermal reaction method. First of all, MXene nanosheets are gradually dispersed into deionized water using ultrasonic dispersion under Ar atmosphere. Then, 0.22 g of (NH<sub>4</sub>)<sub>6</sub>Mo<sub>7</sub>O<sub>24</sub>·4H<sub>2</sub>O is added into the MXene nanosheet dispersion via 0.5 h ultrasonic dispersion for *in situ* anchoring Mo ions. Afterward, 0.76 g of thiourea is incorporated into the above dispersion and homogeneously mixed by 0.5 h magnetic stirring under an Ar atmosphere. The dispersion obtained is transferred into a 50 mL Teflon stainless-steel autoclave and reacted at 200 °C for 12 h. The hierarchical MoS<sub>2</sub>/MXene heterostructure is achieved through centrifugation, followed by multiple washes and vacuum drying. The resulting hierarchical MoS<sub>2</sub>/MXene heterostructures with MoS<sub>2</sub> and MXene weight ratios of 1:1, 1:2, and 1:4 are labeled as MoS<sub>2</sub>/MXene-1, MoS<sub>2</sub>/MXene-2, and MoS<sub>2</sub>/MXene-4, respectively. For comparison, pure MoS<sub>2</sub> nanosheets are prepared under the same conditions but without MXene nanosheets.

### Characterization

The detailed characterizations are described in the [Supplementary Materials](#).

### Electrochemical measurements and desalination measurements

The details of electrochemical measurements and desalination measurements are described in the [Supplementary Materials](#).

## RESULTS AND DISCUSSIONS

### Preparation, morphologies, and structures of MoS<sub>2</sub>/MXene heterostructures

As shown in [Figure 1](#), Ti<sub>3</sub>C<sub>2</sub>T<sub>x</sub> MXene is produced by selectively etching the Al layer in Ti<sub>3</sub>AlC<sub>2</sub> using HF as the etchant. The surface of MXene nanosheets is rich in -F, -OH, and/or -O groups, which can enhance the hydrophilicity performance and provide abundant growth sites for MoS<sub>2</sub> nanosheets. Thus, 2D MXene and MoS<sub>2</sub> nanosheets can form a mutually reinforcing structure to prevent aggregation of the nanosheets. MXene nanosheets act as a robust, hydrophilic and conductive substrate, while MoS<sub>2</sub> ones act as pillars between MXene nanosheets, effectively preventing MXene self-accumulation and providing a pathway for rapid ion transport. Therefore, the obtained hierarchical MoS<sub>2</sub>/MXene heterostructure shows great promise as a promising CDI electrode material.

The synthesized MXene nanosheets exhibit an accordion-like structure [[Supplementary Figure 1A](#)] after selective etching the Al layer in Ti<sub>3</sub>AlC<sub>2</sub> with HF solution, confirming the successful preparation of multi-layered MXene nanosheets. Pure MoS<sub>2</sub> consists of large-sized nanosheets that are randomly stacked and

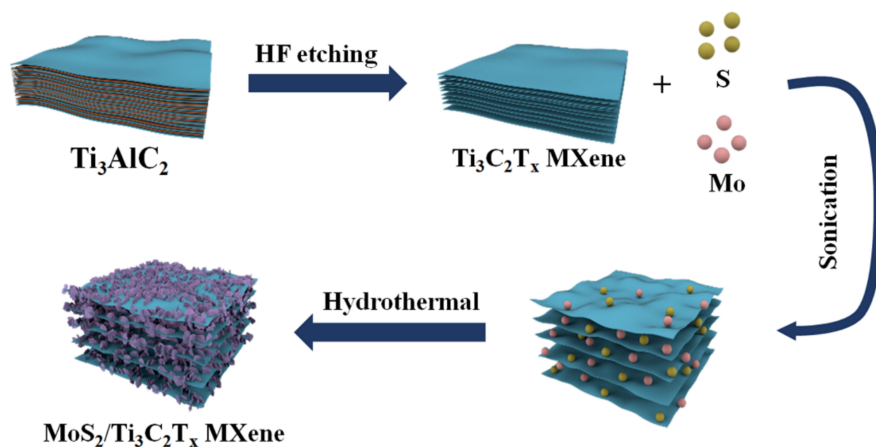


**Figure 1.** Schematic for the preparation of hierarchical  $\text{MoS}_2/\text{MXene}$  heterostructure.  $\text{MoS}_2$ : Molybdenum disulfide.

aggregated into a typical flower-like nanostructure [Supplementary Figure 1B]. However, the hierarchical  $\text{MoS}_2/\text{MXene}$  heterostructures with varying amounts of  $\text{MoS}_2$  loading exhibit different morphologies [Figure 2]. Following a one-step hydrothermal reaction of MXene nanosheets in Mo salt solution, small  $\text{MoS}_2$  nanosheets are uniformly inserted into the interlayers of 2D conductive MXene nanosheets, forming mutually supported architectures. The  $\text{MoS}_2$  nanosheets play a certain role in supporting MXene nanosheets and preventing their restacking. Meanwhile, the anchoring sites provided by MXene nanosheets also restrict the self-stacking of the  $\text{MoS}_2$  nanosheets. Thus, mutually supported architectures formed by MXene nanosheets and  $\text{MoS}_2$  nanosheets can offer abundant active sites for ion adsorption. With an increased dosage of Mo salt, more  $\text{MoS}_2$  nanosheets form on the surface and interlayer of MXene nanosheets. Notably, when the weight ratio is moderate,  $\text{MoS}_2$  nanosheets are uniformly grown on MXene substrate [Figure 2C and D]. However, a further increase in the amount of Mo salt leads to the aggregation of  $\text{MoS}_2$  nanosheets on MXene substrate, as limited growth space hinders their growth [Figure 2E and F]. Thus, an appropriate amount of MXene can effectively inhibit the aggregation of  $\text{MoS}_2$  and MXene nanosheets while providing an open structure that enhances desalination performance.

Furthermore, energy-dispersive X-ray spectroscopy (EDX) mapping of the hierarchical  $\text{MoS}_2/\text{MXene}$  heterostructure [Figure 2G-L] confirms the presence and uniform distribution of Ti, C, Mo, S, and O elements. The  $\text{MoS}_2$  nanosheets are uniformly distributed on the surface and interlayer of MXene nanosheets. A transmission electron microscopy (TEM) image clearly shows the typical layered structures of the heterostructure [Supplementary Figure 2A]. Additionally, a high-resolution TEM (HRTEM) image [Supplementary Figure 2B] provides a detailed view of the layered structure of MXene with 0.28 nm interlayer spacing, corresponding to its (101) plane, and  $\text{MoS}_2$  with 0.68 nm interlayer spacing, corresponding to its (002) plane. This result indicates that  $\text{MoS}_2$  nanosheets have been successfully anchored onto MXene substrate, thereby creating nanoheterogeneous interfaces within the heterostructure.

Figure 3 illustrates the X-ray diffraction (XRD) patterns of  $\text{Ti}_3\text{AlC}_2$ , MXene,  $\text{MoS}_2$  and  $\text{MoS}_2/\text{MXene}$ . In the XRD pattern of  $\text{Ti}_3\text{AlC}_2$ , the peaks at  $9.5^\circ$ ,  $19.1^\circ$ ,  $34.0^\circ$ ,  $39.0^\circ$ ,  $41.8^\circ$ , and  $60.8^\circ$  correspond to (002), (004), (101), (104), (105), and (110) planes of  $\text{Ti}_3\text{AlC}_2$ , respectively. However, the peak at  $39.0^\circ$  disappears after HF etching, indicating the formation of  $\text{Ti}_3\text{C}_2\text{T}_x$ . Importantly, the diffraction peaks shift from  $9.5^\circ$  and  $19.1^\circ$  to  $8.9^\circ$  and  $18.2^\circ$ , respectively. According to the Bragg equation, the interlayer space of MXene nanosheets [(002) plane] increases from 18.6 to 19.7 Å compared with  $\text{Ti}_3\text{AlC}_2$  [Figure 3B]. The expanded interlayer space of MXene can provide large space for anchoring  $\text{MoS}_2$  nanosheets. As shown in Figure 3A, the  $\text{MoS}_2/$

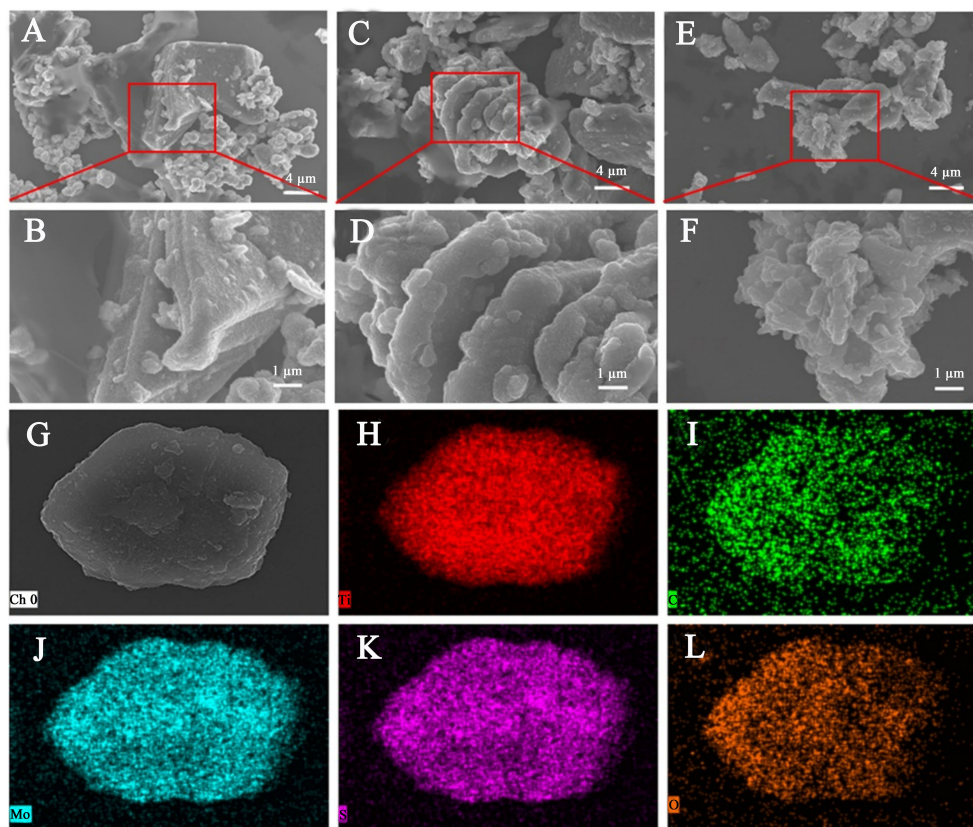


**Figure 2.** SEM images of (A and B) MoS<sub>2</sub>/MXene-1, (C and D) MoS<sub>2</sub>/MXene-2, (E and F) MoS<sub>2</sub>/MXene-4 with low and high magnifications, and EDX mapping of MoS<sub>2</sub>/MXene-2. SEM: Scanning electron microscope; MoS<sub>2</sub>: molybdenum disulfide; EDX: energy-dispersive X-ray spectroscopy.

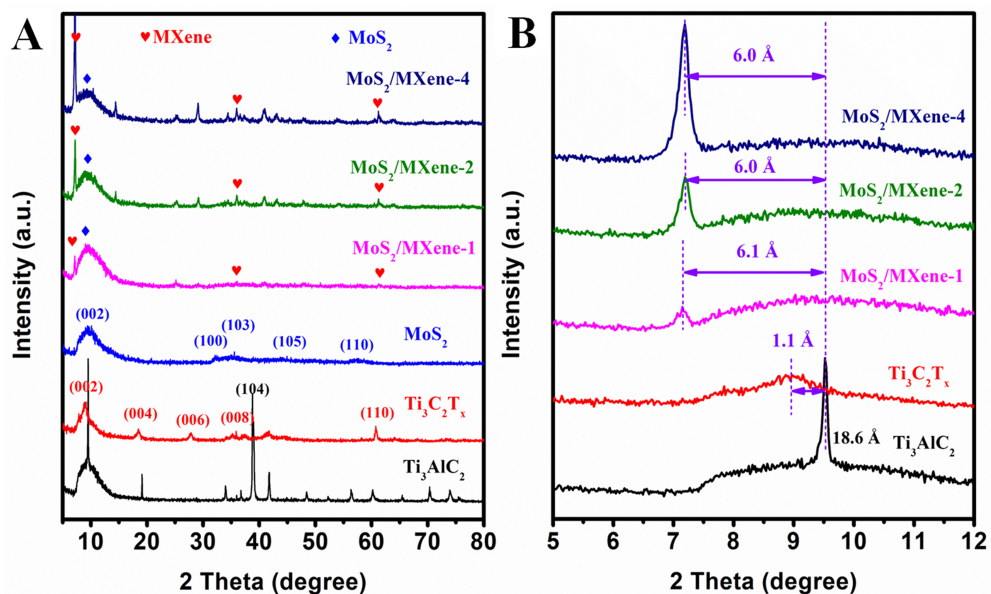


**Figure 3.** XRD patterns of Ti<sub>3</sub>AlC<sub>2</sub>, MXene nanosheets, MoS<sub>2</sub> nanosheets, and hierarchical MoS<sub>2</sub>/MXene heterostructures. XRD: X-ray diffraction; MoS<sub>2</sub>: molybdenum disulfide.

MXene heterostructures exhibit diffraction peaks corresponding to the (002), (004), (006), (008) and (110) planes of MXene, and prominent peaks at  $14^\circ$ ,  $33.8^\circ$ , and  $59.3^\circ$ , which correspond to (002), (100), and (110) planes of  $\text{MoS}_2$  nanosheets, respectively. Thus, the hierarchical  $\text{MoS}_2/\text{MXene}$  heterostructures show characteristic diffraction peaks of both MXene and  $\text{MoS}_2$  nanosheets. Furthermore, XRD patterns reveal a distinct diffraction peak at  $25.4^\circ$ , attributing to the (101) plane of  $\text{TiO}_2$ , indicating that a portion of MXene has undergone oxidation to form  $\text{TiO}_2$  during the hydrothermal process. After the intercalation of  $\text{MoS}_2$  nanosheets, the (002) plane diffraction peak of MXene further shifts, resulting in an increase in layer spacing from 18.6 Å to 24.6–24.7 Å compared to  $\text{Ti}_3\text{AlC}_2$ . The enlarged interlayer spacing is attributed to the exfoliation effect of  $\text{MoS}_2$  nanosheets. The larger layer spacing can provide a larger ion channel, which can facilitate the rapid ion diffusion and improve the ion adsorption rate in the desalination process.

In [Figure 4A](#), the survey scan reveals the existence of C, O, Mo, S, and Ti elements in  $\text{MoS}_2/\text{MXene}$ . The C spectrum [[Figure 4B](#)] shows four main peaks at 288.7, 286.2, 284.5, and 283.2 eV, which are ascribed to C=O, C–O, C–C, and C–Ti–O bonds, respectively. These bonds are associated with  $\text{Ti}_3\text{C}_2$  and incidental carbon. The Ti spectrum [[Figure 4C](#)] exhibits typical peaks at 465.0, 463.0, 461.3, 459.1, 456.7, and 455.2 eV, corresponding to the Ti–O [Ti(III)  $2p_{1/2}$ ],  $\text{Ti}^{3+}$ , Ti–C  $2p_{1/2}$ , Ti–O [Ti(III)  $2p_{3/2}$ ], Ti(II)  $2p_{3/2}$ , and Ti–C  $2p_{3/2}$ , respectively. The Mo spectrum [[Figure 4D](#)] displays distinctive peaks at 231.5 and 228.4 eV, corresponding to Mo  $3d_{3/2}$  and Mo  $3d_{5/2}$  orbitals, indicating the Mo (IV) state in  $\text{MoS}_2/\text{MXene}$ . Besides, two characteristic peaks of Mo 3d at 232.7 and 229.5 eV correspond to Mo–C orbitals, indicating the chemical bonds between  $\text{MoS}_2$  and MXene. Furthermore, the peak of C–S/Ti–S centered at 169.1 eV also indicates the existence of chemical bonds between  $\text{MoS}_2$  and MXene [[Figure 4E](#)]. In [Figure 4F](#), the O spectrum can be deconvoluted into distinct peaks at 529.7, 530.3, 531.3, and 533.1 eV, corresponding to Ti–O, C–Ti–O<sub>x</sub>, C–Ti–(OH)<sub>x</sub> bonds, and H<sub>2</sub>O. Additionally, the weight content of O elements is 24.93% in  $\text{MoS}_2/\text{MXene-2}$  [[Supplementary Table 1](#)]. These abundant oxygenic groups contribute to the superior surface wettability of  $\text{MoS}_2/\text{MXene-2}$ .

### Electrochemical performances of $\text{MoS}_2/\text{MXene}$ heterostructures

[Figure 5A](#) displays cyclic voltammetry (CV) curves of MXene and  $\text{MoS}_2/\text{MXene}$  at a scan rate of  $20 \text{ mV}\cdot\text{s}^{-1}$  in the potential range of  $-0.8$  to  $0.4 \text{ V}$ . The CV curve of MXene shows no distinct redox peak and has a distorted rectangular shape, indicating the contribution of electrical double-layer capacitance in MXene electrode. However, the CV curves of  $\text{MoS}_2/\text{MXene}$  with different  $\text{MoS}_2$  nanosheet loadings exhibit minor redox peaks between  $-0.3$  and  $-0.1 \text{ V}$ , indicating the pseudocapacitance behavior of  $\text{MoS}_2$  nanosheets. The region enclosed by these curves within the potential range represents the relative specific capacitance. As shown in [Figure 5A](#), the areas under the CV curves of  $\text{MoS}_2/\text{MXene}$  are larger than that of MXene. Among them,  $\text{MoS}_2/\text{MXene-2}$  has the largest area, suggesting the highest specific capacitance. The superior electrochemical performance of  $\text{MoS}_2/\text{MXene-2}$  can be attributed to the enhanced hydrophilicity and conductivity and offered by MXene, along with the optimized amount of  $\text{MoS}_2$  nanosheets. The CV curves of MXene and  $\text{MoS}_2/\text{MXene}$  heterostructures at different scan rates are shown in [Figure 5B–E](#). All these curves present rectangular mirror images, indicating excellent electrochemical behavior at diverse scan rates. Moreover, a noticeable increase in current density was observed with higher scan rates. Analysis of the CV curves indicates that  $\text{MoS}_2/\text{MXene-2}$  also has the best specific capacitances among the tested materials at the respective scan rates [[Figure 5F](#)]. The improved specific capacitance can be ascribed to multiple factors. Firstly, the interconnected framework formed by the combination of  $\text{MoS}_2$  and MXene nanosheets promotes charge transfer in the hierarchical  $\text{MoS}_2/\text{MXene}$  heterostructure. Additionally, the *in situ* anchoring effect of MXene provides growth sites for  $\text{MoS}_2$  nanosheets, effectively inhibiting the self-aggregation of  $\text{MoS}_2$  and MXene nanosheets, while also offering more exposed redox sites.

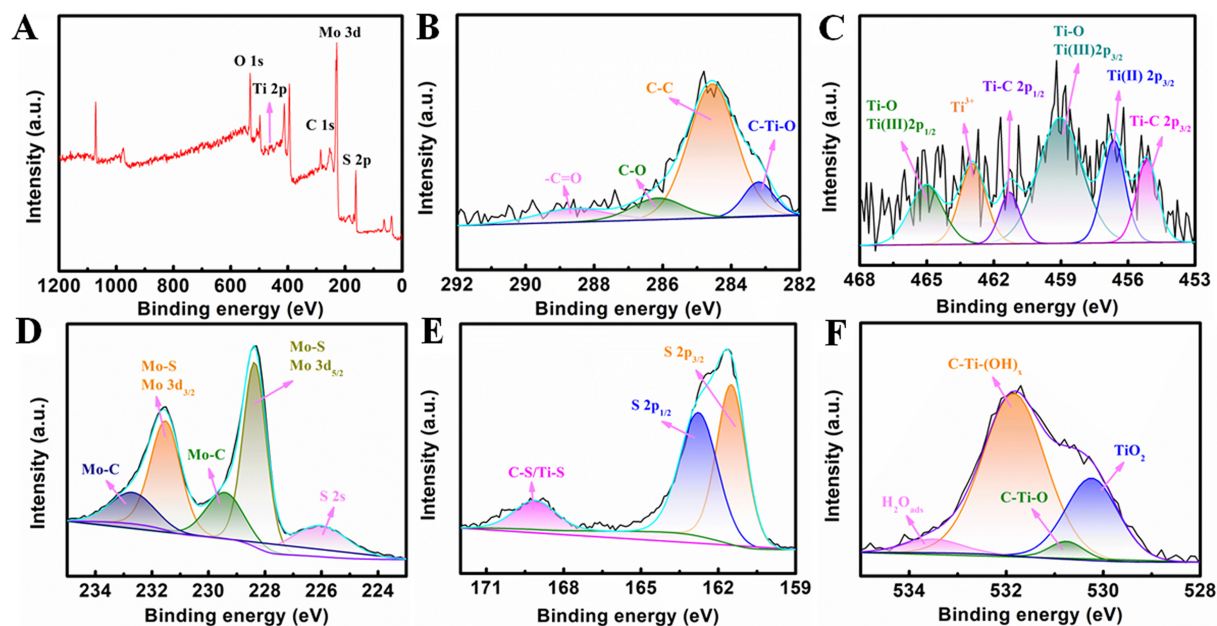


**Figure 4.** XPS characterization of the hierarchical MoS<sub>2</sub>/MXene-2 heterostructures: (A) XPS survey spectrum; (B) high-resolution spectra of C 1s; (C) Ti 2p; (D) Mo 3d; (E) S 2p; (F) O 1s. XPS: X-ray photoelectron spectroscopy; MoS<sub>2</sub>: molybdenum disulfide.

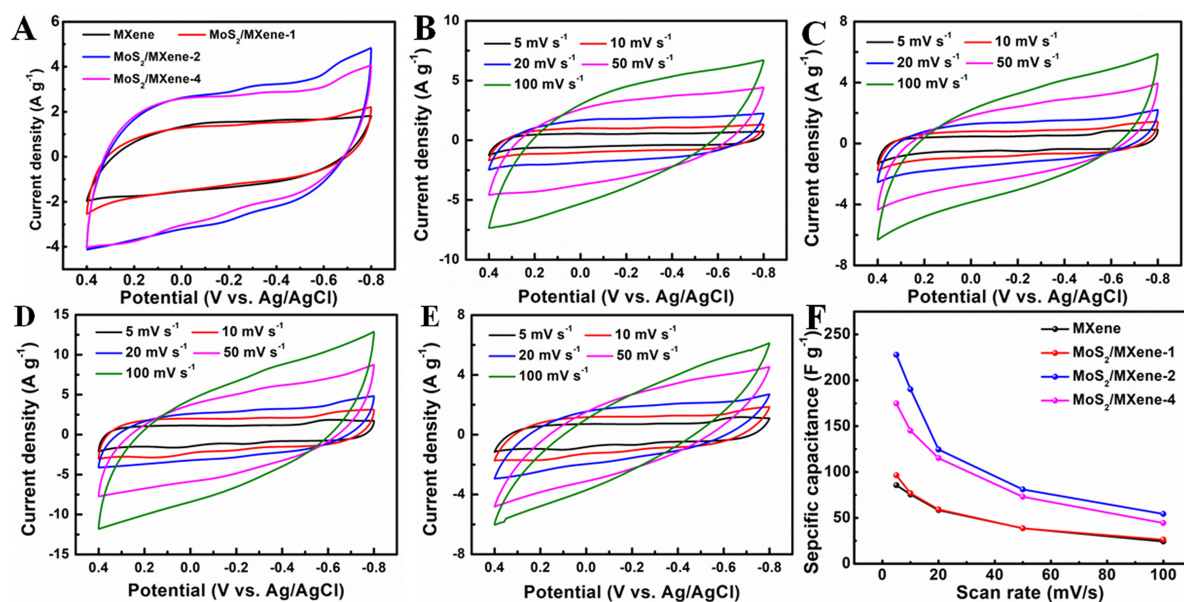


**Figure 5.** (A) CV curves of MXene and MoS<sub>2</sub>/MXene heterostructure electrodes at a scan rate of 20 mV s<sup>-1</sup>; (B) CV curves of MXene, (C) MoS<sub>2</sub>/MXene-1, (D) MoS<sub>2</sub>/MXene-2, (E) MoS<sub>2</sub>/MXene-4 at various scan rates; (F) the specific capacitances calculated from CV curves. CV: Cyclic voltammetry; MoS<sub>2</sub>: molybdenum disulfide.

The galvanostatic charge-discharge (GCD) curves at a current density of 2 A·g<sup>-1</sup> are shown in [Figure 6A](#). The specific capacitances of MXene, MoS<sub>2</sub>/MXene-1, MoS<sub>2</sub>/MXene-2, and MoS<sub>2</sub>/MXene-4 electrodes calculated from these curves are 37.8, 50.3, 171.8, and 124.7 F·g<sup>-1</sup>, respectively. The trend in the GCD performances agrees with the findings from the CV curves. [Figure 6B-E](#) exhibits GCD curves at varying current densities, and [Figure 6F](#) summarizes the specific capacitances calculated from these GCD curves.

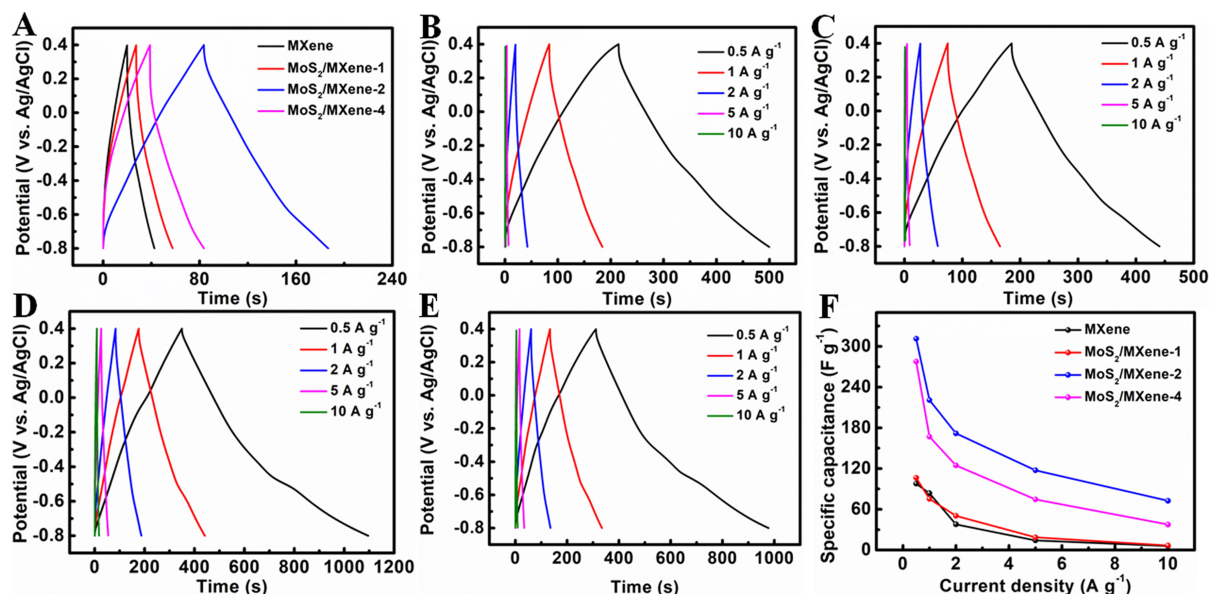


**Figure 6.** (A) Charge/discharge curves of MXene and hierarchical MoS<sub>2</sub>/MXene heterostructure electrodes at a current density of 2 A g<sup>-1</sup>; Charge/discharge curves of (B) MXene, (C) MoS<sub>2</sub>/MXene-1, (D) MoS<sub>2</sub>/MXene-2, (E) MoS<sub>2</sub>/MXene-4 at various current densities; (F) the specific capacitances calculated from charge/discharge curves. MoS<sub>2</sub>: Molybdenum disulfide.

Clearly, the MoS<sub>2</sub>/MXene-2 electrode shows the best electrochemical performance. For comparison, a pure MoS<sub>2</sub> electrode was also examined as a reference measuring by CV and GCD curves [Supplementary Figure 3]. The CV curves of MoS<sub>2</sub> indicate the presence of pseudocapacitance in MoS<sub>2</sub>. The specific capacitance of MoS<sub>2</sub>, determined from the CV curves, rises with increasing scan rates. Similarly, the specific capacitance of MoS<sub>2</sub>, derived from the GCD curves [Supplementary Figure 3C], increases with increasing current densities. Nevertheless, regardless of the calculation method used, the electrochemical performance of MoS<sub>2</sub> is inferior to that of MXene and MoS<sub>2</sub>/MXene heterostructure electrodes.

Electrochemical impedance spectroscopy (EIS) was further explored to analyze the conductive performance and electron/ion transport behaviors at the electrodes/electrolyte interface. As seen in [Supplementary Figure 4], all Nyquist plots exhibit subtle arcs in high-frequency regions and linear trends in low-frequency regions. In low-frequency regions, a steeper line indicates faster ion diffusion within the electrode. The high-frequency arc is associated with electronic resistance, while the subtle arc likely results from charge transfer resistance. MoS<sub>2</sub>/MXene-2 electrode shows the lowest surface resistance (3.2 Ω), while the MXene, MoS<sub>2</sub>/MXene-1, MoS<sub>2</sub>/MXene-2 and MoS<sub>2</sub>/MXene-4 ones exhibit resistance values of 9.4, 4.9, and 4.7 Ω, respectively. The charge transfer resistance (R<sub>ct</sub>) of MoS<sub>2</sub>/MXene-2 electrode shows 4.4 Ω by fitting the equivalent circuit, while MXene, MoS<sub>2</sub>/MXene-1, and MoS<sub>2</sub>/MXene-4 exhibit resistance values of 10.3, 5.9, and 5.5 Ω, respectively. This demonstrates that the incorporation of MoS<sub>2</sub> nanosheets into the MXene can reduce both the surface resistance and charge transfer resistance. The presence of MoS<sub>2</sub> nanosheets acts as pillars, effectively inhibiting the aggregation of MXene and expanding its interlayer distance. Therefore, MoS<sub>2</sub>/MXene heterostructure electrodes show lower resistance compared to pure MXene electrodes.

### CDI performances of MoS<sub>2</sub>/MXene heterostructures

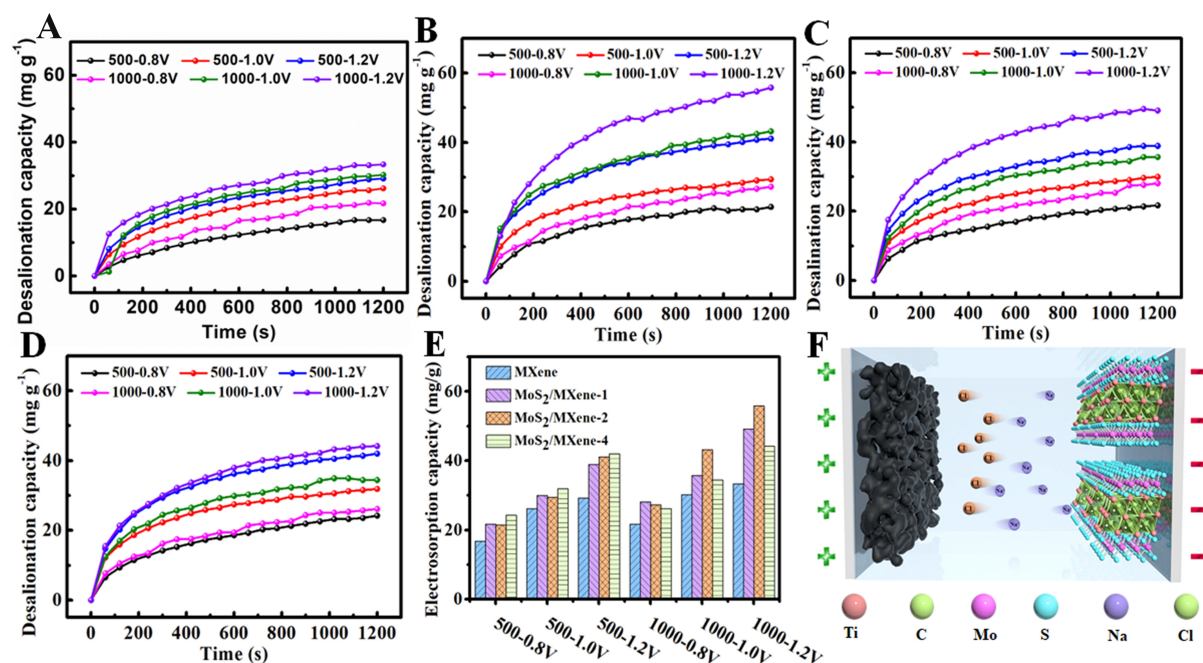
Surface wettability is essential for the penetration of electrolytes into electrode materials, thus influencing CDI performance. As seen in [Supplementary Figure 5], MXene nanosheets exhibit hydrophilic (water contact angle = 26.5°) as a result of the abundance of oxygenic groups and fluorine groups from their surface. On the other hand, MoS<sub>2</sub> nanosheets are hydrophobic, with a water contact angle of 112.1°. The

introduction of hydrophilic MXene significantly reduces the water contact angle of the hierarchical MoS<sub>2</sub>/MXene heterostructure. The improved surface wettability can enhance the utilization of the active sites and further increase the desalination capacity and desalination rate.

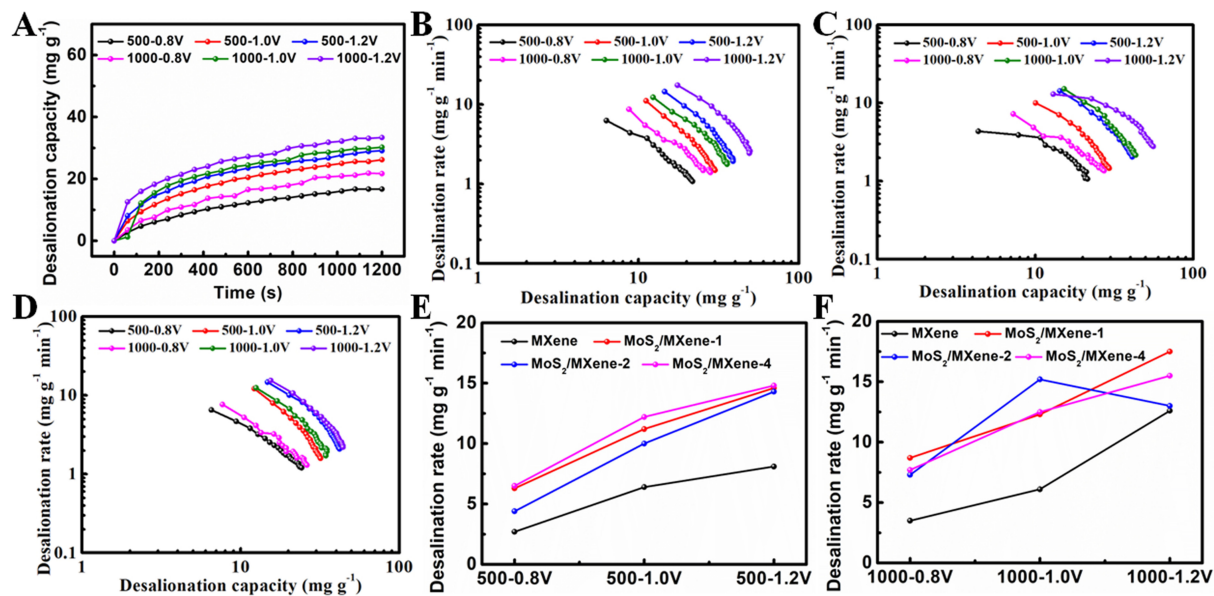
To assess the desalination performances, desalination experiments were conducted in batch mode using different voltages/concentrations in NaCl solution. Prior to evaluating the desalination performance, the changes in NaCl solution conductivity at varied concentrations were initially studied. A conductivity meter was used to test the conductivity of NaCl solutions with specified concentrations. Subsequently, the relationship between the concentration of NaCl solution and their conductivity at room temperature was established [Supplementary Figure 6]. As shown in Figure 7A-E and Supplementary Figure 7, the desalination capacities increase significantly with the applied voltage. Moreover, higher desalination capacities are generated at higher conductivities of the NaCl solution. Several factors contribute to the enhanced desalination performance. Primarily, the high voltage can not only facilitate the ion transport and diffusion into the inner layers of MXene and MoS<sub>2</sub> nanosheets but also increase the active sites for ion adsorption. The high conductivity of NaCl solution means not only high NaCl concentration but also more ions and a large concentration gradient. Thus, all these factors facilitate the enhancement of desalination capacity. As shown in Figure 7E, the desalination capacities of hierarchical MoS<sub>2</sub>/MXene heterostructure devices are much higher than those of MXene devices and MoS<sub>2</sub> devices [Supplementary Figure 7B], and the MoS<sub>2</sub>/MXene-2 device exhibits the highest desalination capacity (up to 55.8 mg·g<sup>-1</sup> at a voltage of 1.2 V and an initial conductivity of 1,000 μS·cm<sup>-1</sup>). These results suggest that the MoS<sub>2</sub>/MXene-2 device exhibits the optimal candidate for CDI.

Figure 7F shows the CDI behavior of hierarchical MoS<sub>2</sub>/MXene heterostructure anode and cathode. In the CDI desalination process, Na<sup>+</sup> ions are intercalated into the MXene and MoS<sub>2</sub> nanosheet interlayer, while Cl<sup>-</sup> ions are intercalated into the active carbon. As mentioned in the previous analysis discussion, MoS<sub>2</sub>/MXene-2 exhibits an optimized hierarchical structure characterized by even distribution of MoS<sub>2</sub> nanosheets on MXene, along with increased exposed active edges. The highly hydrophilic MXene serves as a conductive substrate, which can reduce the ion diffusion paths. Besides, the pillar effect of MoS<sub>2</sub> can greatly inhibit the restacking of MXene and enlarge its interlayer distance. Furthermore, the *in situ* anchoring effect of MXene guides the growth of MoS<sub>2</sub> nanosheets, effectively preventing their restacking. For MoS<sub>2</sub>/MXene-4, only a few MoS<sub>2</sub> nanosheets are dispersed on the surface and between the layers of MXene, resulting in a reduced number of active sites for desalination. Thus, the desalination capacity of MoS<sub>2</sub>/MXene-4 devices is 49.1 mg·g<sup>-1</sup> at 1.2 V. In the case of MoS<sub>2</sub>/MXene-1, excess MoS<sub>2</sub> nanosheets result in self-aggregation, reducing the MoS<sub>2</sub> edges. So, the desalination capacity of MoS<sub>2</sub>/MXene-1 devices is 44.2 mg·g<sup>-1</sup> at 1.2 V. Therefore, MoS<sub>2</sub>/MXene-2 shows the best desalination performance due to the uniform distribution of MoS<sub>2</sub> nanosheets and conductive and hydrophilic MXene substrate.

The Kim-Yoon-Ragone method is employed for further study of the kinetical performance of MXene and hierarchical MoS<sub>2</sub>/MXene heterostructure devices for CDI systems. As seen in Figure 8, the average desalination rate rises with the voltage escalation at the same initial conductivity, and the average desalination rate also climbs with the initial conductivity at the same voltage. Besides, the desalination rates of the hierarchical MoS<sub>2</sub>/MXene heterostructure devices are much higher than those of the MXene device. The maximum desalination rate of MoS<sub>2</sub>/MXene-2 devices reaches 15.2 mg·g<sup>-1</sup>·min<sup>-1</sup> at 1 V, while the desalination rates of MXene, MoS<sub>2</sub>/MXene-1, and MoS<sub>2</sub>/MXene-4 devices are 6.1, 12.3, and 12.5 mg·g<sup>-1</sup>·min<sup>-1</sup>, respectively. These findings further demonstrate that hierarchical MoS<sub>2</sub>/MXene heterostructures can improve the kinetical performance for CDI process. Besides, the cycling performance of MoS<sub>2</sub>/MXene-2 heterostructure devices is shown in Supplementary Figure 8. After 30 cycles, the



**Figure 7.** The desalination capacity and time curves of (A) MXene, (B) MoS<sub>2</sub>/MXene-1, (C) MoS<sub>2</sub>/MXene-2, (D) MoS<sub>2</sub>/MXene-4 devices in NaCl solution; (E) The desalination capacities and (F) the CDI working process of MXene and hierarchical MoS<sub>2</sub>/MXene heterostructure devices. MoS<sub>2</sub>: Molybdenum disulfide.



**Figure 8.** Ragone plots of (A) MXene, (B) MoS<sub>2</sub>/MXene-1, (C) MoS<sub>2</sub>/MXene-2, (D) MoS<sub>2</sub>/MXene-4 devices; The maximum desalination rate-voltage curves at the initial conductivity of (E) 500  $\mu\text{S}\cdot\text{cm}^{-1}$  and (F) 1000  $\mu\text{S}\cdot\text{cm}^{-1}$ . MoS<sub>2</sub>: Molybdenum disulfide.

desalination capacity decreases to 27.5  $\text{mg}\cdot\text{g}^{-1}$ , and the retention rate is 79.4%. Additionally, the desalination performances of hierarchical MoS<sub>2</sub>/MXene heterostructures are compared with MXene or MoS<sub>2</sub>-based composite CDI devices reported previously [Supplementary Table 2]. The desalination performances of hierarchical MoS<sub>2</sub>/MXene heterostructures in this work outperform those of other MXene or MoS<sub>2</sub>-based composite devices.

## CONCLUSIONS

Ti<sub>3</sub>C<sub>2</sub>T<sub>x</sub> MXene nanosheets were utilized as a conductive and wettable skeleton for fabricating hierarchical MoS<sub>2</sub>/MXene heterostructures. In the hierarchical MoS<sub>2</sub>/MXene heterostructures, the pillar-supported MoS<sub>2</sub> nanosheets play a critical role in preventing restacking of MXene and enlarging the interlayer spacing of MXene to enhance ion storage capacity. Additionally, the *in situ* anchoring effect of MXene effectively prevents restacking of MoS<sub>2</sub> nanosheets and increases MoS<sub>2</sub> active edges. The hierarchical MoS<sub>2</sub>/MXene heterostructure with well-distributed and active edge-rich MoS<sub>2</sub> nanosheets demonstrates a high specific capacitance of 171.8 F·g<sup>-1</sup> at 2 A·g<sup>-1</sup>. Moreover, the optimized MoS<sub>2</sub>/MXene heterostructure device for CDI exhibits an excellent desalination capacity of 55.8 mg·g<sup>-1</sup>. Therefore, the high conductive MXene-supported nanosized MoS<sub>2</sub> shows great potential as low-cost electrode materials in the field of CDI.

## DECLARATIONS

### Authors' contributions

Funding acquisition, resources, methodology, formal analysis, data curation, writing-original draft, review and editing: Zhang Y

Methodology, formal analysis, investigation, validation, data curation: Li X

Formal analysis: Xi W

Data curation: Zhang Q

Data curation: Ge X

Writing-review and editing: You J, Zhang Q, Shi D

Funding acquisition, resources, supervision, writing-review and editing: Jin J

### Availability of data and materials

Not applicable.

### Financial support and sponsorship

The authors gratefully acknowledge the financial support from the National Natural Science Foundation of China (Nos. 51903040 and 52203340), Scientific Research Program of Department of Education in Hubei Province, and Overseas Expertise Introduction Center for Discipline Innovation (No. D18025).

### Conflicts of interest

All authors declared that there are no conflicts of interest.

### Ethical approval and consent to participate

Not applicable.

### Consent for publication

Not applicable.

### Copyright

© The Author(s) 2024.

## REFERENCES

1. Deng D, Aouad W, Braff WA, Schlumpberger S, Suss ME, Bazant MZ. Water purification by shock electro dialysis: deionization, filtration, separation, and disinfection. *Desalination* 2015;357:77-83. [DOI](#)
2. Xu X, Allah AE, Wang C, et al. Capacitive deionization using nitrogen-doped mesostructured carbons for highly efficient brackish water desalination. *Chem Eng J* 2019;362:887-96. [DOI](#)
3. Zhao D, Lee LY, Ong SL, Chowdhury P, Siah KB, Ng HY. Electro dialysis reversal for industrial reverse osmosis brine treatment. *Sep Purif Technol* 2019;213:339-47. [DOI](#)

4. Xi W, Jin J, Zhang Y, et al. Hierarchical MXene/transition metal oxide heterostructures for rechargeable batteries, capacitors, and capacitive deionization. *Nanoscale* 2022;14:11923-44. DOI
5. Cai Y, Zhang L, Fang R, Wang Y, Wang J. Maximized ion accessibility in the binder-free layer-by-layer MXene/CNT film prepared by the electrophoretic deposition for rapid hybrid capacitive deionization. *Sep Purif Technol* 2022;292:121019. DOI
6. Vafakhah S, Beiramzadeh Z, Saeedikhani M, Yang HY. A review on free-standing electrodes for energy-effective desalination: recent advances and perspectives in capacitive deionization. *Desalination* 2020;493:114662. DOI
7. Chen B, Feng A, Deng R, Liu K, Yu Y, Song L. MXene as a cation-selective cathode material for asymmetric capacitive deionization. *ACS Appl Mater Interfaces* 2020;12:13750-8. DOI
8. Zhang W, Liu Y, Jin C, et al. Efficient capacitive deionization with 2D/3D heterostructured carbon electrode derived from chitosan and g-C<sub>3</sub>N<sub>4</sub> nanosheets. *Desalination* 2022;538:115933. DOI
9. Zhu W, Lin Y, Kang W, et al. An aerogel adsorbent with bio-inspired interfacial adhesion between graphene and MoS<sub>2</sub> sheets for water treatment. *Appl Surf Sci* 2020;512:145717. DOI
10. Xu L, Ding Z, Chen Y, et al. Carbon nanotube bridged nickel hexacyanoferrate architecture for high-performance hybrid capacitive deionization. *J Colloid Interface Sci* 2023;630:372-81. DOI
11. Tan Z, Wang W, Zhu M, et al. Ti<sub>3</sub>C<sub>2</sub>T<sub>x</sub> MXene@carbon dots hybrid microflowers as a binder-free electrode material toward high capacity capacitive deionization. *Desalination* 2023;548:116267. DOI
12. Cai Y, Zhang W, Fang R, Zhao D, Wang Y, Wang J. Well-dispersed few-layered MoS<sub>2</sub> connected with robust 3D conductive architecture for rapid capacitive deionization process and its specific ion selectivity. *Desalination* 2021;520:115325. DOI
13. Cai Y, Zhang W, Zhao J, Wang Y. Flexible structural construction of the ternary composite Ni,Co-Prussian blue analogue@MXene/polypyrrole for high-capacity capacitive deionization. *Appl Surf Sci* 2023;622:156926. DOI
14. El-deen AG, El-kholly HK, Ali MEM, et al. Polystyrene sulfonate coated activated graphene aerogel for boosting desalination performance using capacitive deionization. *Sep Purif Technol* 2022;299:121760. DOI
15. Yang X, Jiang H, Zhang W, et al. A novel “butter-sandwich” Ti<sub>3</sub>C<sub>2</sub>T<sub>x</sub>/PANI/PPY electrode with enhanced adsorption capacity and recyclability toward asymmetric capacitive deionization. *Sep Purif Technol* 2021;276:119379. DOI
16. Wang H, Wei D, Gang H, et al. Hierarchical porous carbon from the synergistic “pore-on-pore” strategy for efficient capacitive deionization. *ACS Sustainable Chem Eng* 2020;8:1129-36. DOI
17. Liu Y, Wang K, Xu X, et al. Recent advances in faradic electrochemical deionization: system architectures versus electrode materials. *ACS Nano* 2021;15:13924-42. DOI PubMed
18. Dixit F, Zimmermann K, Dutta R, et al. Application of MXenes for water treatment and energy-efficient desalination: a review. *J Hazard Mater* 2022;423:127050. DOI
19. Lei J, Xiong Y, Yu F, Ma J. Flexible self-supporting CoFe-LDH/MXene film as a chloride ions storage electrode in capacitive deionization. *Chem Eng J* 2022;437:135381. DOI
20. Srimuk P, Halim J, Lee J, Tao Q, Rosen J, Presser V. Two-dimensional molybdenum carbide (MXene) with divacancy ordering for brackish and seawater desalination via cation and anion intercalation. *ACS Sustainable Chem Eng* 2018;6:3739-47. DOI
21. Zhu G, Chen L, Lu T, et al. Cu-based MOF-derived architecture with Cu/Cu<sub>2</sub>O nanospheres anchored on porous carbon nanosheets for efficient capacitive deionization. *Environ Res* 2022;210:112909. DOI PubMed
22. Yu L, Tao X, Feng S, et al. Recent development of three-dimension printed graphene oxide and MXene-based energy storage devices. *Tungsten* 2024;6:196-211. DOI
23. Ihsanullah I. MXenes (two-dimensional metal carbides) as emerging nanomaterials for water purification: progress, challenges and prospects. *Chem Eng J* 2020;388:124340. DOI
24. Li B, Sun K, Xu W, et al. Tailoring interlayer spacing in MXene cathodes to boost the desalination performance of hybrid capacitive deionization systems. *Nano Res* 2023;16:6039-47. DOI
25. Wang S, Li Z, Wang G, Wang Y, Ling Z, Li C. Freestanding Ti<sub>3</sub>C<sub>2</sub>T<sub>x</sub> MXene/Prussian blue analogues films with superior ion uptake for efficient capacitive deionization by a dual pseudocapacitance effect. *ACS Nano* 2022;16:1239-49. DOI PubMed
26. Qie H, Liu M, Fu X, et al. Interfacial charge-modulated multifunctional MoS<sub>2</sub>/Ti<sub>3</sub>C<sub>2</sub>T<sub>x</sub> penetrating electrode for high-efficiency freshwater production. *ACS Nano* 2022;16:18898-909. DOI PubMed
27. Wang K, Chen L, Zhu G, et al. Ferroferric oxide@titanium carbide MXene heterostructure with enhanced sodium storage ability for efficient hybrid capacitive deionization. *Desalination* 2022;522:115420. DOI
28. Gong S, Liu H, Zhao F, et al. Vertically aligned bismuthene nanosheets on MXene for high-performance capacitive deionization. *ACS Nano* 2023;17:4843-53. DOI
29. Mateen A, Ahmad Z, Ali S, et al. Silicon intercalation on MXene nanosheets towards new insights into a superior electrode material for high-performance Zn-ion supercapacitor. *J Energy Storage* 2023;71:108151. DOI
30. Chen Z, Xu X, Wang K, et al. Hybrid of pyrazine based  $\pi$ -conjugated organic molecule and MXene for hybrid capacitive deionization. *Sep Purif Technol* 2023;315:123628. DOI
31. Wang L, Liu Z, Wang Z, et al. Up-shifting the desalination rate limit of capacitive deionization via integrating chloride-capturing Bi nanocluster with flow-through cell architecture. *Chem Eng J* 2023;460:141726. DOI
32. Chen Z, Xu X, Liu Y, et al. Ultra-durable and highly-efficient hybrid capacitive deionization by MXene confined MoS<sub>2</sub> heterostructure. *Desalination* 2022;528:115616. DOI
33. Hao Z, Cai Y, Wang Y, Xu S, Wang J. A coupling technology of capacitive deionization and MoS<sub>2</sub>/nitrogen-doped carbon spheres

- with abundant active sites for efficiently and selectively adsorbing low-concentration copper ions. *J Colloid Interface Sci* 2020;564:428-41. DOI
34. Liu Y, Du X, Wang Z, et al. MoS<sub>2</sub> nanoflakes-coated electrospun carbon nanofibers for “rocking-chair” capacitive deionization. *Desalination* 2021;520:115376. DOI
  35. Nguyen TKA, Wang TH, Doong R. Architectures of flower-like MoS<sub>2</sub> nanosheet coated N-doped carbon sphere electrode materials for enhanced capacitive deionization. *Desalination* 2022;540:115979. DOI
  36. Peng W, Wang W, Han G, Huang Y, Zhang Y. Fabrication of 3D flower-like MoS<sub>2</sub>/graphene composite as high-performance electrode for capacitive deionization. *Desalination* 2020;473:114191. DOI
  37. Tian S, Zhang X, Zhang Z. Novel MoS<sub>2</sub>/NOMC electrodes with enhanced capacitive deionization performances. *Chem Eng J* 2021;409:128200. DOI
  38. Xi W, Zhang Y, Wang R, et al. The effect of electrode thickness and electrode/electrolyte interface on the capacitive deionization behavior of the Ti<sub>3</sub>C<sub>2</sub>T<sub>x</sub> MXene electrodes. *J Alloys Compd* 2023;947:169701. DOI